(Received 29 November 2024, Accepted 25 February 2025, Scheduled 8 March 2025)

Research on Multi-Field Information of Transformer with Harmonic Invasion in Offshore Wind Farm Based on Electromagnetic-Solid-Acoustic Coupling

Chao Pan[1], Tongrui Fu[1,*], Jingge An[1], and Diyao Jiang[2]

[1] *Key Laboratory of Modern Power System Simulation and Control & Renewable Energy Technology Ministry of Education (Northeast Electric Power University), Jilin 132012, China*
[2] *State Grid Zhejiang Electric Power Co., Ltd. Zhoushan Power Supply Company, Zhoushan 316000, ZheJiang, China*

ABSTRACT: Aiming at the operation stability of transformer with harmonic invasion in offshore wind farm, the evolution and propagation of electromagnetic-solid-acoustic information are studied. Combined with the measured data of invasive harmonic currents, it is found that the proportions of the 5th and 7th harmonics are larger than those of other harmonics. A multi-physical field propagation and information extraction method for transformer is proposed based on the principle of electromagnetic-solid-acoustic coupling. Then, the magnetic density, force, vibration, and noise characteristics of components with harmonic invasion are analyzed. The results show that the increase of harmonics intensifies the vibration and noise of transformer in the same load. In the same harmonic proportion, the waveform distortion of the multi-physical characteristic parameters caused by the 7th harmonic is more significant than the 5th. Moreover, the vibration and noise intensify with rising load factor in the same harmonic invasion mode. Meanwhile, the dynamic experimental platforms are built to measure multi-physics field information in different modes. By comparing the experimental data and simulation result, the accuracy of proposed method can be verified. Furthermore, the 5th harmonic is selected as the typical characterization parameter to study the mapping relationship between harmonics and vibration characteristics. The criteria for disturbed destabilization are formulated, providing new ideas for the life cycle operation and maintenance of offshore wind transformer.

1. INTRODUCTION

As an important clean energy source, offshore wind energy resources have attracted much attention due to their adequacy. The vigorous development of offshore wind power represents an inevitable trend of global power grid development in the future. More and more power electronic devices are connected to the grid and become the main harmonic sources in offshore wind farms [1]. The long submarine cables connected to offshore wind turbines have a greater capacitance to ground than the overhead lines used in onshore wind farms [2, 3]. Therefore, long-distance submarine cables are easily influenced by harmonic amplification effects. As key equipment in offshore wind power system, the reliable operation of the transformer is significant to the safety of substation. When harmonics invade from the grounding point, transformer takes unstable performance [4–6]. The situation includes abnormalities such as current distortion, excitation saturation, and increased losses, which even endanger the operating life of equipment. Harmonic invasion produces serious magnetostrictive effect, which will lead to uneven stress distribution and vibration intensification. Furthermore, increased noise is led by increased vibration, resulting in the internal structural stability of the transformer. In addition, harmonic invasion can lead to problems such as degradation of power quality and false operation of protective devices.

In [7], the principle of the background harmonic amplification caused by submarine cable integration is analyzed, and a mitigation scheme by installing shunt filters is proposed. In [8], by discussing the resonance amplification due to the distribution parameters of submarine cables, a cascaded notch-filter-based active damping method is proposed to suppress the harmonic resonance. However, none of the above literature has studied the harm caused by harmonics in offshore wind farm to transformer. In [9], a significant increase in the AC loss of high-temperature superconducting transformer is analyzed under the influence of high harmonics. In [10], the effects of different nonlinear loads on a three phase distribution transformer are examined, and additional power losses are calculated. In [11], the effect of transformer parameters on harmonic resonance frequency in offshore wind farm is investigated by sensitivity analysis. In [12], the impact of the offshore transformer equivalent resistance on resonance damping is investigated.

In summary, existing literature mainly focuses on the offshore wind power harmonic resonance problem and the effect of harmonics on transformer. However, the variation laws of internal multi-field (electromagnetic field, solid force field and acoustic field) information in transformer with harmonic invasion have not been deeply explored. The impact of harmonics and methods for identifying characteristic information also

* Corresponding author: Tongrui Fu (664373986@qq.com).

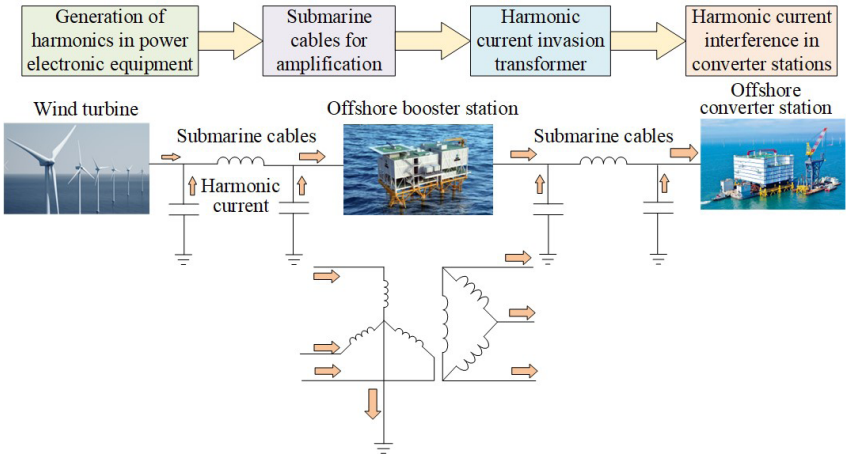

FIGURE 1. Transformer with harmonic invasion.

need to be researched. Meanwhile, the current sensing means for transformer monitoring mainly relies on electric measurements. How unobservable abnormal vibration and noise can be represented by observable harmonic current and load factor is significant.

In this paper, aiming at the transformer with harmonic invasion in offshore wind farm, the variation characteristics of multi-field information in transformer are investigated. Based on the principle of electromagnetic-solid-acoustic coupling, a multi-physical field propagation and information extraction method for transformer is proposed. Electromagnetic-solid-acoustic coupling is the coupling of internal field information. Then, the abnormal phenomenon of transformer is caused by the change in internal multi-field information with harmonic invasion.

Firstly, the pathway of harmonic invasion in offshore wind power transformer is investigated in this paper. Harmonic characteristics are analyzed through measured data, focusing on interference effects of typical harmonics. Then, an information extraction method is proposed based on electromagnetic-solid-acoustic coupling. Taking a Yd-wired three-phase transformer as example, the variation laws of transformer multi-field information under different harmonic invasion modes are studied and revealed. Finally, dynamic experiment platforms are built to measure feature parameters such as current, vibration, and noise. The effectiveness of the proposed method can be verified by the consistency between simulation and experiments. On this basis, the mathematical mapping relationship between harmonics and transformer vibration is constructed, and the instability criterion is further formed, which provides a basis for harmonic interference identification and suppression. Appropriate harmonic suppression strategies are facilitated by this study, thus improving the ability of transformer to resist harmonic interference.

2. PRINCIPLE OF HARMONIC INVASION GROUNDING TRANSFORMER IN OFFSHORE WIND FARM

In offshore wind farm, significant harmonic is generated by the widespread application of power electronic equipment and the parallel operation of multiple units. Then, harmonics are amplified by long-distance submarine cables and invade the neutral point of the transformer through earth.

Studies have shown that the harmonic currents generated by offshore wind farm contain harmonic components of multiple frequencies [13]. Harmonic currents may lead to the oversaturation of core excitation, resulting in increased losses and elevated temperatures. Meanwhile, harmonics will intensify the skin effect of transformer, affecting the safe and stable operation. The principle of harmonic invasion is shown in Fig. 1.

Based on the measured data of an offshore wind farm, the harmonic currents of the $1^{\#}$ main transformer (140 MVA/220 kV) in the booster station are analyzed in this paper. Despite a harmonic suppression unit being installed on site, harmonic components continue to invade the transformer through the neutral point. The statistical data of the number of days per month that harmonic currents invaded during the period of 2023–2024 are presented, with the typical components illustrated in Fig. 2(a). It is obvious that the invasion of harmonic currents is frequent but irregular, in which the 5th and 7th harmonics occur with a relatively high frequency. Furthermore, a typical time period in May 2024 is selected to analyze the current monitoring data at the neutral point of transformer, as shown in Fig. 2(b). It is found that the harmonic current at neutral point varies drastically. Taking phase B as an example, the current spectrum is shown in Fig. 2(c). It is clear that the low-frequency components account for the major part, among which the 5th and 7th harmonic contents are relatively larger. Therefore, this study focuses on the investigation of the 5th and 7th harmonics.

3. MULTI-FIELD PROPAGATION AND INFORMATION EXTRACTION OF TRANSFORMER WITH HARMONIC INVASION

Based on electromagnetic-solid-acoustic coupling, a multi-field information extraction method for harmonic invasion transformer is proposed. A multi-field propagation mathemat-

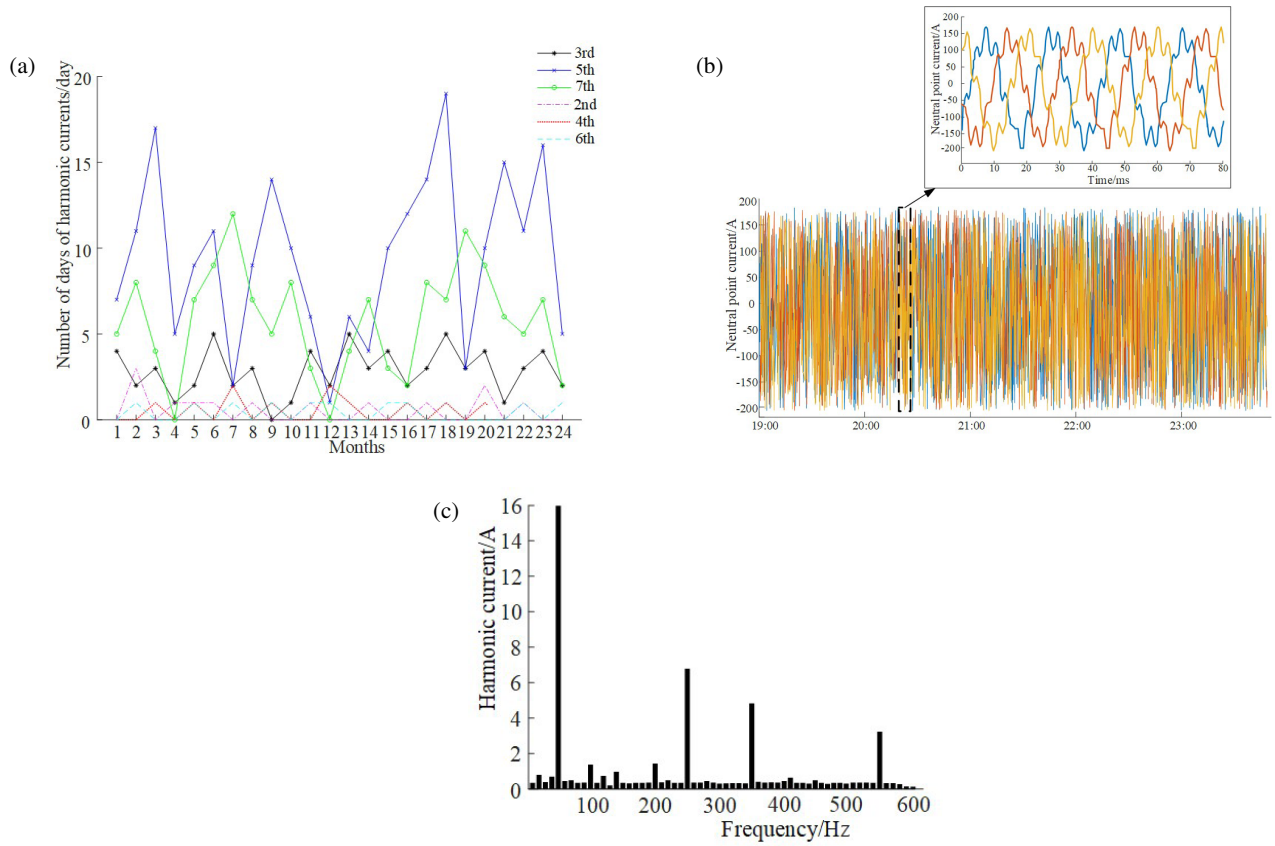

FIGURE 2. Measured data. (a) Daily data statistics of typical harmonic current, (b) monitoring data of harmonic current in typical period, (c) B phase current spectrum diagram.

ical model is developed as follows:

$$\begin{cases} \mathbf{MS} = (\mathbf{S}_e, \mathbf{S}_s, \mathbf{S}_a) \\ \mathbf{Input} = (\mathbf{Input}_e, \mathbf{Input}_s, \mathbf{Input}_a) \\ \mathbf{Output} = (\mathbf{Output}_e, \mathbf{Output}_s, \mathbf{Output}_a) \end{cases} \tag{1}$$

$$\begin{cases} \dot{\mathbf{MS}}_e = \mathbf{MS}_e(t_k, i, B) + \mathbf{X} \cdot \mathbf{Input}_e(t_k, U_{AC}, \xi) \\ \mathbf{Output}_e(t_k, i, B, F) = \alpha \cdot \dot{\mathbf{MS}}_e \\ \dot{\mathbf{MS}}_s = \mathbf{MS}_s(t_k, g) + \mathbf{Y} \cdot \mathbf{Input}_m(t_k, \xi_{e-s}) \\ \mathbf{Output}_s(t_k, g) = \beta \cdot \dot{\mathbf{MS}}_s \\ \dot{\mathbf{MS}}_a = \mathbf{MS}_a(t_k, p) + \mathbf{Z} \cdot \mathbf{Input}_a(t_k, \xi_{s-a}) \\ \mathbf{Output}_a(t_k, p) = \gamma \cdot \dot{\mathbf{MS}}_a \end{cases} \tag{2}$$

$$\begin{cases} \chi = (I_h, \beta) \\ \xi = (\xi_{e-s}, \xi_{s-a}) = (F, g) \end{cases} \tag{3}$$

where **MS** is the mode-state matrix of system which contains electromagnetic mode-state matrix $\mathbf{MS}_e$, mode-state matrix of solid mechanics $\mathbf{MS}_s$, and acoustic mode-state matrix $\mathbf{MS}_a$. The multi-field information is extracted through the solution of an electromagnetic-solid-acoustic coupling model. **Input** is the system input matrix which contains electromagnetic input matrix $\mathbf{Input}_e$, solid mechanics input matrix $\mathbf{Input}_s$, and acoustic input matrix $\mathbf{Input}_a$. **X**, **Y**, and **Z** are the input coefficient matrices for each field. U_{AC} is the sinusoidal AC excitation. χ is the control parameter matrix which contains harmonic current I_h and load factor β. ξ is the coupling correlation parameter, containing electromagnetic-solid coupling parameter $\xi_{e-s}(F)$ and solid-acoustic coupling parameter $\xi_{s-a}(g)$. **Output** is the system output matrix that contains multi-field output matrix $\mathbf{Output}_e$, $\mathbf{Output}_m$, and $\mathbf{Output}_a$. α, β, and γ are extracting matrices, which extract the multi-field feature parameters (current, magnetic flux, electromagnetic force, vibration and noise) from **MS**.

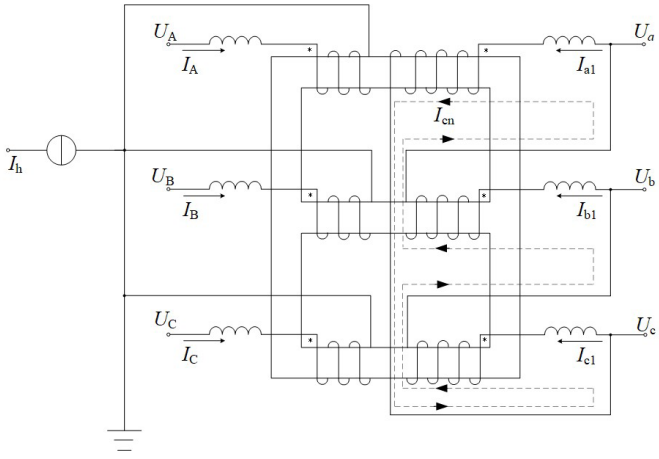

FIGURE 3. Circuit model.

3.1. Electromagnetic Information

The circuit model of three-phase transformer with harmonic invasion is shown in Fig. 3, where U_A, U_B, and U_C are the primary side voltages; I_A, I_B, and I_C are the primary side currents; U_a, U_b, and U_c are the secondary side voltages; and I_{a1}, I_{b1}, and I_{c1} are the secondary side currents. Meanwhile, the harmonic current I_h in offshore wind farm is considered in the model.

$$\begin{aligned} I_A(t) &= I_f(t) + I_h(t) \\ &= I_1 \sin(\omega t) + \sum_{d=2}^{n} I_d \sin(d\omega t) \\ \Phi_A(t) &= \Phi_f(t) + \Phi_h(t) \\ &= \Phi_1 \sin(\omega t) + \sum_{d=2}^{n} \Phi_d \sin(d\omega t) \end{aligned} \tag{4}$$

where I_A is the winding current; Φ_A is the core flux; I_f and Φ_f are the fundamental components; I_h and Φ_h are the harmonic components; I_1 is the current amplitude corresponding to the fundamental; I_d is the current amplitude corresponding to the dth harmonic; Φ_1 is the core flux corresponding to the fundamental; Φ_d is the core flux corresponding to the dth harmonic; Ω is the angular frequency of the fundamental; d is the number of harmonics.

Taking phase A as an example, I_A and Φ_A after harmonic invasion can be expressed as the superposition of I_f, I_h and Φ_f, Φ_h. When the harmonic current varies, the frequency of the winding current and main flux variations deviates from the power frequency.

A nonlinear magnetic field model for transformers is constructed [14]:

$$\begin{aligned} \mathbf{J}_A &= \frac{I_A(t)}{S} = \frac{I_f(t) + I_h(t)}{S} \\ &= \frac{I_1 \sin(\omega t) + \sum_{d=2}^{n} I_d \sin(dwt)}{S} \end{aligned} \tag{5}$$

where $\mathbf{J}_A$ is the current density of the phase A winding, and S is the area of the winding cross-section.

The electromagnetic field of the transformer can be solved using the edge finite element method (EFEM). The basic solution unit of EFEM is the prismatic edge element. The annulus $\mathbf{A}_e$ of the edge e is taken as the degree of freedom of the edge element, and the vector shape function $\mathbf{n}_e$ is used. The interpolation function of unit is obtained:

$$\mathbf{A} = \sum_{e=1}^{u_{\text{edge}}} \mathbf{n}_e \mathbf{A}_e \tag{6}$$

where u_{edge} is the total number of edge element, and $\mathbf{A}$ is the vector magnetic potential.

Furthermore, the model is solved by Galerkin method of weighted residuals [15, 16]:

$$G_A = \iiint_V \frac{1}{\mu} (\nabla \times \mathbf{M}_w) \cdot (\nabla \times \mathbf{M}_w) \, \mathbf{A} dV - \iiint_V \mathbf{M}_w \cdot \mathbf{J}_A dV \tag{7}$$

where G_A is the magnetic field Galerkin residual with harmonic invasion, $\mathbf{M}_w$ the vector weight function, and μ the permeability. Further derivations can be found in Appendix A.

The G_A equation is discretized, resulting in a system of algebraic equations that can be solved to obtain A. The field information is further calculated using $\mathbf{A}$, including magnetic flux density $\mathbf{B}$ and magnetic field energy $\mathrm{d}W_e$:

$$\begin{cases} \mathbf{B} = \nabla \times \mathbf{A} \\ dW_e = \dfrac{1}{2} \displaystyle\int d\mathbf{B} \cdot d\mathbf{H} \end{cases} \tag{8}$$

3.2. Vibration and Noise Information

The electromagnetic force on the transformer windings can be decomposed into axial and radial components [17]. The axial electromagnetic force is mainly analyzed in this study. The axial force on the winding unit is shown in Fig. 4.

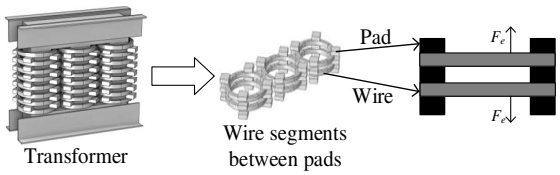

FIGURE 4. Simplify the basic unit of wind.

The stiffness characteristics of insulation pads vary with the magnitude of the winding pre-tightening force. When the pre-tightening force is constant, stiffness characteristics can be considered linear. The result was obtained based on electromagnetic coupling:

$$\mathbf{F}_e = \sum^{n_s} \int \mathbf{J}_A \times \mathbf{B} dV \tag{9}$$

where $\mathbf{F}_e$ is the winding force, and n_s is the number of winding units.

The electromagnetic force on the component can be computed through the solved parameters (magnetic flux density $\mathbf{B}$ and electromagnetic energy) in electromagnetic model.

The axial force on the winding can be extracted using Equation (10) [18]:

$$\mathbf{F}_z = \frac{\partial W_e}{\partial z} = \frac{1}{\mu} \int \mathbf{B} \frac{\partial \mathbf{B}}{\partial z} dV \tag{10}$$

where $\mathbf{F}_z$ is the electromagnetic force on the winding in the direction z.

The axial electromagnetic force $\mathbf{F}_z$ is analyzed considering the composition of the winding current under harmonic intrusion. Under the excitation of power frequency, the variation

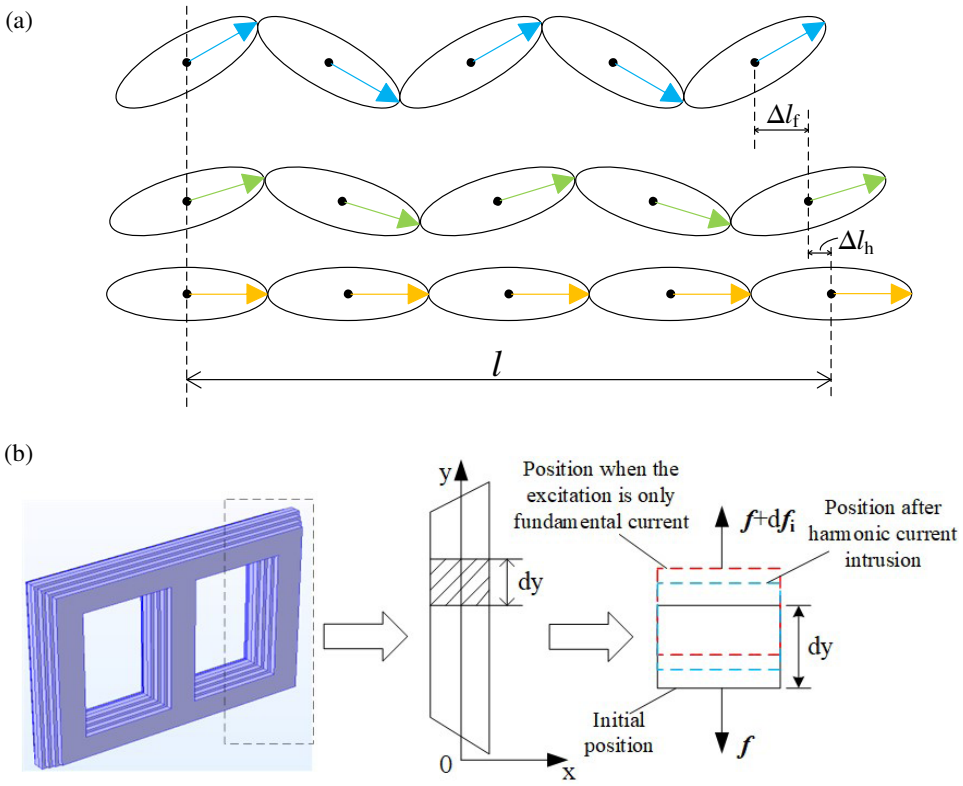

FIGURE 5. Basic principle of iron core vibration. (a) The basic principle of magnetostrictive effect, (b) core axial vibration model.

frequency of the axial electromagnetic force in the winding is 100 Hz. There are high-frequency harmonic components in the axial force on the winding coils with harmonic invasion.

$$\mathbf{F}_z = \mathbf{F}_f + \mathbf{F}_h = 0.5\mathbf{B}I_1^2(1+\cos(2\omega t)) + \mathbf{F}_h \tag{11}$$

where $\mathbf{F}_f$ is the electromagnetic force corresponding to the fundamental, and $\mathbf{F}_h$ is the electromagnetic force corresponding to the harmonic.

Due to the magnetostrictive characteristics of silicon steel sheet, the iron core vibrates. The equivalent model of core vibration with harmonic invasion is shown in Fig. 5. Under the action of power frequency sinusoidal current I_f, the arrangement of the ferromagnetic material is increased by Δl_f. The length of arrangement is extended by Δl_h with the harmonic current I_h. Therefore, the magnetostriction coefficient λ at the invasion of harmonic currents is deduced as follows:

$$\lambda = \frac{\Delta l_f + \Delta l_h}{l} \tag{12}$$

Considering the magnetostrictive effect, the relationship among relative permeability, tensile stress, and magnetic flux density is as follows:

$$\Delta\mu = -\frac{2\lambda_s \kappa \mu^2}{\mathbf{B}_s^2} \tag{13}$$

$$\mathbf{B}_\kappa = (\mu + \Delta\mu)\mathbf{H} + \lambda\kappa \tag{14}$$

where μ is the magnetic permeability, $\Delta\mu$ the relative magnetic permeability, κ the tensile stress, λ_s the magnetostriction coefficient under magnetic saturation, $\mathbf{B}_s$ the saturation magnetic induction, $\mathbf{B}_\kappa$ the magnetic induction with tensile stress, and $\mathbf{H}$ the magnetic field intensity.

$\mathbf{f}$+d$\mathbf{f_i}$ is the force on the cross section of core column. Neglecting the damping effect of the transformer structure, the core vibration equation is obtained based on the mechanical theory [19]:

$$ES_c\frac{\partial^2\mathbf{u}(y,t)}{\partial y^2} + \mathbf{f}(y,t) = \rho_c S_c\frac{\partial^2\mathbf{u}(y,t)}{\partial t^2} \tag{15}$$

where E is the Young's modulus; $\partial\mathbf{u}/\partial y$ is the axial strain; $\mathbf{f}(y,t)$ is the magnetostrictive force on this mass unit; y and t are position and time, respectively; ρ_c is the iron core density; S_c is the cross-sectional area.

Based on the solid force model, the axial displacement $\mathbf{x}$ is calculated, and subsequently the component vibration acceleration g is solved during harmonic invasion:

$$g = \frac{d^2\mathbf{x}}{dt^2} \tag{16}$$

When the components of transformer vibrate, acoustic waves propagate into the surrounding fluid. The g obtained from Equation (16) is used as the excitation input to the acoustic model to realize the vibration-noise coupling calculation.

$$-\mathbf{n}\cdot\left[-\frac{1}{\rho_a}(\nabla(p_b+p_t)-\mathbf{q})\right] = -\mathbf{n}\cdot g \tag{17}$$

where ρ_a is the fluid density, p_b the background sound pressure, p_t the transformer noise sound pressure, and $\mathbf{q}$ the dipole do-

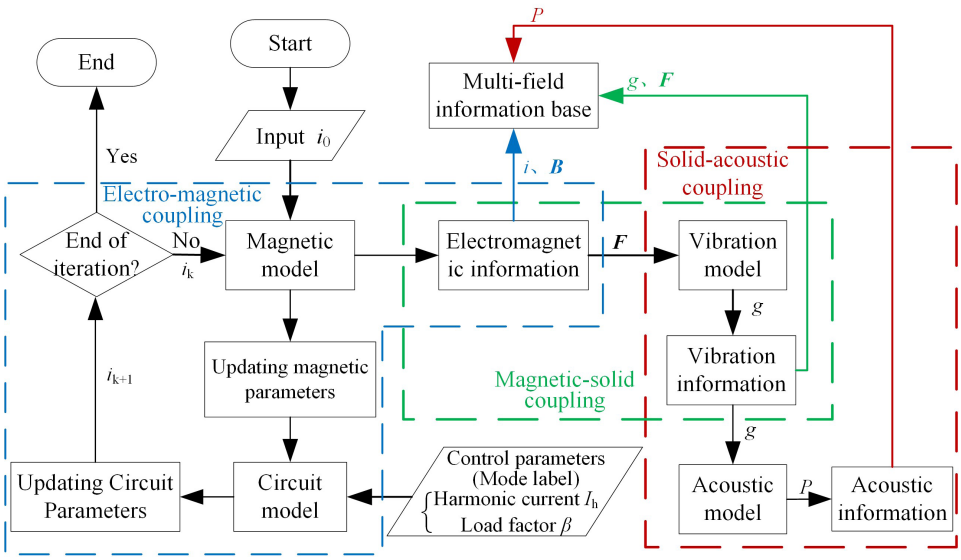

FIGURE 6. Electromagnetic-solid-acoustic coupling model.

main source. Solve the internal acoustic equations of the transformer:

$$\frac{1}{\rho_a v^2}\cdot\frac{\partial^2(p_b+p_t)}{\partial^2 t}+\nabla\cdot\left[-\frac{1}{\rho_a}(\nabla(p_b+p_t)-\mathbf{q})\right]=\mathbf{Q} \quad (18)$$

where v is the speed of sound, and $\mathbf{Q}$ is the unipolar domain source.

The sound pressure level L_p is utilized to analyze the sound pressure variations:

$$L_p=20\cdot\lg\left(\frac{P}{P_f}\right) \quad (19)$$

where P is the valid value of sound pressure, and P_f is the reference value of sound pressure, which is generally taken as 20 μPa.

3.3. Information Extraction Based on Electromagnetic-Solid Acoustic Coupling

Based on the principle of information propagation in electromagnetic-solid-acoustic multi-field domains, a method for information extraction is proposed, which is shown in Fig. 6. The steps are as follows:

1) Electromagnetic coupling: Taking time as an indexing parameter, the electromagnetic information at t_k is acquired. The winding current i_k at t_k is used as the excitation input to the current-carrying domain and the magnetic connected domain. Meanwhile, control parameters (harmonic current I_h and load factor β) are entered. The electromagnetic spatial-temporal distribution of transformer is solved to obtain the feature information such as magnetic density $\mathbf{B}$.

(2) Electromagnetic-solid coupling: Based on the magnetic field information obtained from the electromagnetic coupling model, the electromagnetic force $\mathbf{F}_k$ of the component at t_k is calculated. In the mechanical vibration domain, $\mathbf{F}_k$ is taken as an excitation to obtain the vibration acceleration g_k of winding and core.

(3) Solid-acoustic coupling: In the multi-field information base, vibration acceleration g_k of the component at t_k is extracted. In the acoustic propagation domain, g_k is input as an excitation to obtain the sound pressure P_k.

4) Iterative process of information extraction: t_k is used as link index, and the solution is made in the order of the magnetic-solid-acoustic physical evolution mechanism. Taking the control parameters I_h and β as mode labels, the field feature information and control parameters are associated and stored in the multi-field information base. Then, the field parameters at the next moment are updated. When the absolute convergence norm is less than the preset criterion value, or the number of iterations does not reach the upper limit, multi-field solution is carried out at t_{k+1}, and vice versa the iteration ends.

Utilizing the proposed information extraction method, the multi-field spatio-temporal distribution of transformer components is investigated.

4. SIMULATION

In combination with the actual operation of large three-phase transformer, a custom-made experimental transformer BSS-1000VA with a scaled-down proportion is constructed, as shown in Fig. 13. The primary and secondary windings are star-delta connected, and the specific parameters of transformer are shown in Table 1. Based on the electromagnetic-solid-acoustic model, simulation analysis is carried out, and key information parameters are extracted.

4.1. Pre-Procedure

Simulation analysis of transformer is conducted using the COMSOL finite element software. Then, the geometric modeling tool integrated in simulation software is used to build

TABLE 1. Transformer arguments.

Parameters	Rated value	Measured value
Capacity S_N /VA	1000	—
Frequency/Hz	50	—
Voltage U_N/V	35/220	—
No-load current I_0/A	0.1	0.1
Core size/mm^3	—	300×150×190
Young's modulus of silicon steel sheet/MPa	1.95×10^5	1.93×10^5
Poisson's ratio of silicon steel sheet	0.25	0.26
Young's modulus of winding coils/Mpa	0.81	0.80
Poisson's ratio of winding coils	0.36	0.37

TABLE 2. Typical harmonic interference parameter table.

Interference mode / Parameters		Actual measured I_h amplitude and proportion (A/%)	I_h amplitude of the simulation and proportion (A/%)
harmonic-free	m0	0	0
5th harmonic	m1	12/5%	0.09/5%
	m2	21/10%	0.15/10%
7th harmonic	m3	21/10%	0.15/10%

transformer model. The transformer model is refined by using free tetrahedral mesh for mesh dissection.

The complexity of transformer structural materials in industrial production is significant. Therefore, simplifications are made to the core, windings, and other components in the simulation process to enhance the stability and efficiency of numerical calculations:

(1) Material parameters of winding and core are obtained by tensile-compression test (See Appendix A for experimental platform) and linearized.

(2) The air gap among the platens, clamps, and core silicon steel sheets is ignored.

The different physical fields are preprocessed as follows:

(a) In electromagnetic coupling, three-phase current is input to the coil as excitation for the electromagnetic model. The parallel outer boundary condition of magnetic induction is applied to the magnetic connected domain, while the other boundary conditions are set as the natural boundaries.

(b) In electromagnetic-solid coupling, the base of transformer is set as fixed constraint considering the axial vibration of the components, while the other parts are set as default constraints.

(c) In solid-acoustic coupling, the ambient background sound pressure is set to 0 Pa. Extraneous environmental noise is negligible. With the sound propagation boundary set to be a perfectly matched layer, sound reflection and refraction errors of sound are ignored.

Three harmonic interference modes are established based on the actual harmonics, as shown in Table 2.

The effects of I_h on the electromagnetic, vibration and noise characteristics of the transformer are investigated in different load modes (β is defined as load factor, $\beta = 25\%$, 50%, 75%, 100%). The effects of various harmonic components on transformer parameters at $\beta = 100\%$ are shown in Appendix B. The arrangement of test points ①–④ takes into account the structure features of the core and winding, as shown in Fig. 7. Meanwhile, through a large amount of data calibration, the simulation model is debugged so that the simulation model has high accuracy.

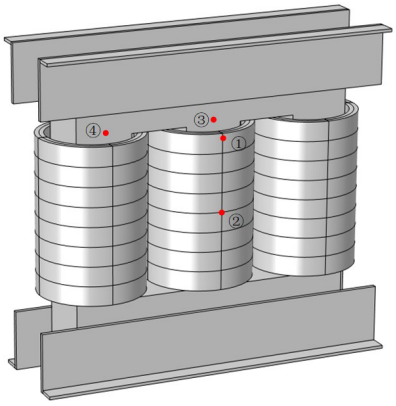

FIGURE 7. Simulation model.

4.2. Simulation Results of Winding

Taking phase B as an example, the variation of electromagnetic information in different modes is analyzed. Magnetic flux leakage of winding B_σ is shown in Fig. 8, and partial winding currents and main magnetic density results are shown in Appendix B.

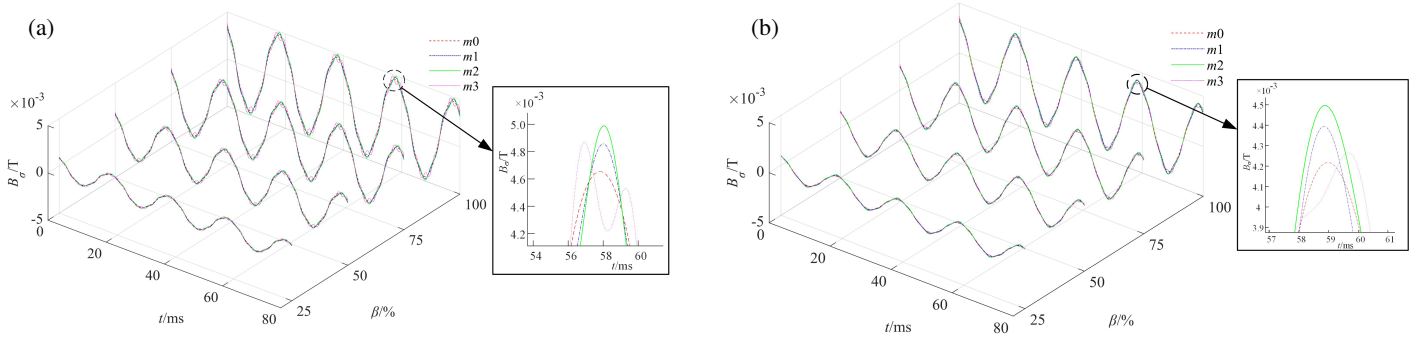

FIGURE 8. Magnetic leakage information of test points. (a) Test point ①, (b) test point ②.

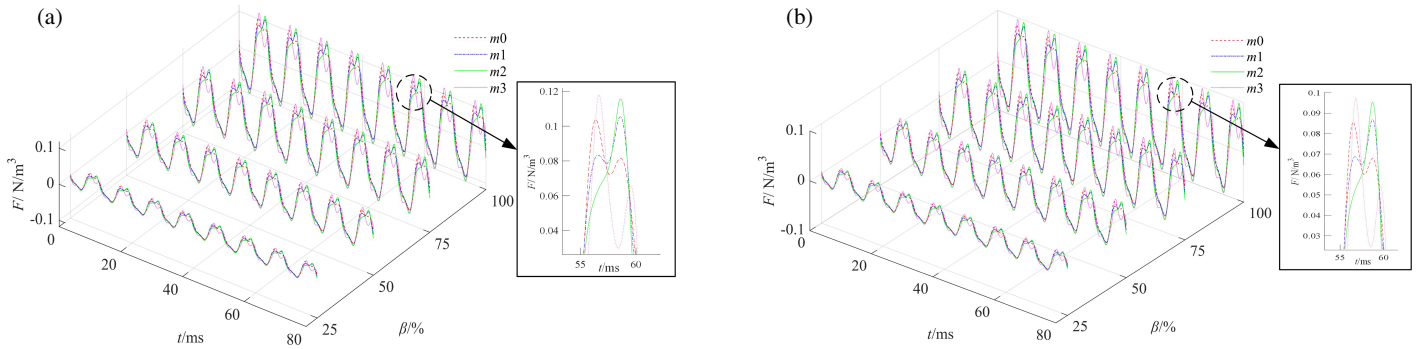

FIGURE 9. Force information of test points on winding. (a) Test point ①, (b) test point ②.

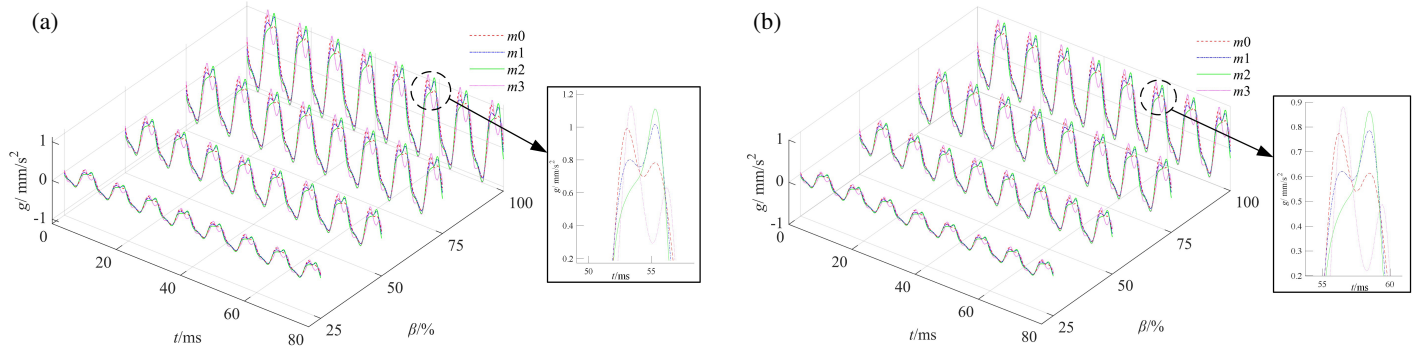

FIGURE 10. Vibration information of test points on winding. (a) Test point ①, (b) test point ②.

As shown in Fig. 8, the effect of harmonic on winding current and leakage under loading operation is not significant. While the time domain fluctuations of B_σ are mainly concentrated in the crest region. Taking the m3 mode as an example, when β is increased from 25% to 100%, the amplitude of leakage $B_{\sigma\_\max}$ at test point ① increases by 2.5 times, and that at test point ② rises by 2.3 times. Moreover, B_σ at the terminal of winding is greater than the middle part. It is easy to find that $B_{\sigma\_\max}$ increases with the load factor.

Under full-load operation, the $B_{\sigma\_\max}$ of the test point in m2 mode is about 1.1 times that of the m0 mode, and the $B_{\sigma\_\max}$ of the test point in m1 mode is about 1.05 times that of the m0 mode. The time domain waveform of B_σ is similar to a sine wave for constant β. Moreover, the waveform distortion of B_σ is more severe in m3 mode than that in m2 mode for the same harmonic content. At the same frequency, the waveform distortion of B_σ in m2 mode is more significant than that in m1 mode. For the same I_h, the distortion of B_σ is more prominent as β increases. As a result, the waveform of B_σ can be distorted due to harmonic invasion, and the leakage of winding is consistent with the trend of current change.

The forces and vibrations of winding are investigated, and the simulation results are shown in Fig. 9 and Fig. 10.

In Fig. 9 and Fig. 10, it can be seen that the vibration frequency of the winding in the m0 mode is twice that of the power frequency. With I_h invasion the force and vibration frequency of the winding is slightly larger than 100 Hz. The above simulation results are consistent with the conclusions of the theoretical analysis. Under full-load operation, the electromagnetic force F and amplitude of vibration acceleration $g_{\max}$ in m2 mode are

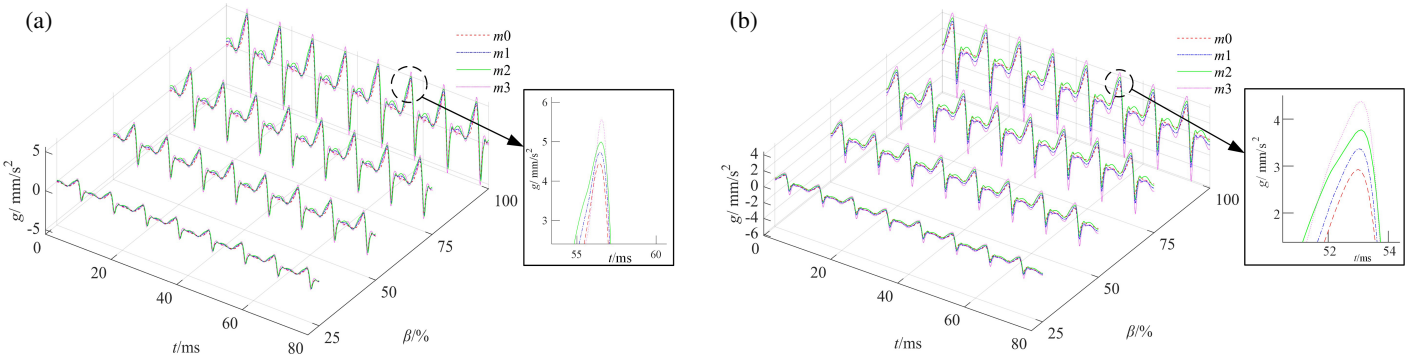

FIGURE 11. Vibration information of test points on iron core. (a) Test point ③, (b) test point ④.

TABLE 3. Maximum noise on transformer surface.

Noise \ Scenario information	Mode-state	β/%			
		25	50	75	100
$L_{p\,\max}$ (dB)	m0	28.3	29.0	30.2	31.0
	m1	28.6	29.6	30.5	31.6
	m2	29.3	30.5	31.7	32.9
	m3	30.8	31.2	32.6	33.8

approximately 1.1 times that of the m1 mode. Compared with the m2 mode, vibration in the m3 mode is more intense. As a result, the enhancement of both F and $g_{\max}$ of the winding is led to by the increased I_h content in loading modes. Additionally, F and $g_{\max}$ distortions are exacerbated by elevated I_h frequencies. The vibration abnormality at the end of the winding is more prominent than that in the middle, which is consistent with the leakage characteristics of the winding.

4.3. Simulation Results of Iron Core

The test points ③ and ④ were selected on the main core column (phase B) and side column (phase A) of the transformer to analyze the vibration, and the results are shown in Fig. 11.

In Fig. 11, when β is increased from 25% to 100%, the $g_{\max}$ of the main column is increased by 2.4 times, and the $g_{\max}$ of the side column is intensified by 2.1 times. Under the same harmonic frequency, the $g_{\max}$ of the m2 mode is about 1.2 times higher than that of m1 mode. Under the same harmonic content, the degree of waveform distortion in the m3 mode is greater than that in the m2 mode. When β is 100% and operates in m3 mode, $g_{\max}$ at test point ③ is about 1.3 times that of test point ④. The main core column vibrates more obviously than the side columns. As a result, the $g_{\max}$ of iron core is enhanced by an increase in the harmonic content under the same frequency of I_h. Increasing frequency at the same harmonic content of I_h leads to more severe g-waveform distortion. Core vibration is more intense with increasing load factor in the same mode. Comparing Fig. 11 with Fig. 10, the vibration of the core is more intense than those of the winding due to the magnetostrictive effect.

4.4. Simulation Results of Noise

The maximum sound pressure level $L_{p\,\max}$ at the surface of the transformer for different modes is shown in Table 3.

As shown in Table 3, the noise of transformer in each mode increases as β rises, and the variation law of noise is consistent with the vibration. For the same β, $L_{p\,\max}$ in m3 mode increases by approximately 8% compared to the m0 mode, while $L_{p\,\max}$ in the m2 mode increases by about 5% relative to the m0 mode.

Taking β =100% as an example, m0 and m3 modes are selected to analyze the time domain variation of the transformer body noise. The distribution of $L_{p\,\max}$ at the moment of maximum noise is shown in Fig. 12.

The results show that for the same β, an increase in transformer noise is caused by I_h. For the same I_h, the sound pressure level of the core is higher than that of the winding, which is consistent with the results of the vibration simulation. $L_{p\,\max}$ exhibits a positive correlation with the proportion and frequency of I_h.

By simulating and analyzing the effects of harmonics on the electromagnetic-solid-acoustic multi-field of the transformer, the following laws are summarized:

(1) With harmonic invasion, all physical fields of winding are interfered. The magnetic flux leakage, force, and vibration acceleration show similar laws of variation. With the same harmonic mode, as the load factor increases, the change of multi-field information becomes more significant, which intensifies the influence of harmonic on the transformer. Under the same load mode, vibration and noise are enhanced by the increase of harmonic components. With increasing frequency, the time-domain waveforms of the winding current, vibration, and noise become more distorted. Magnetic flux leakage and vibration

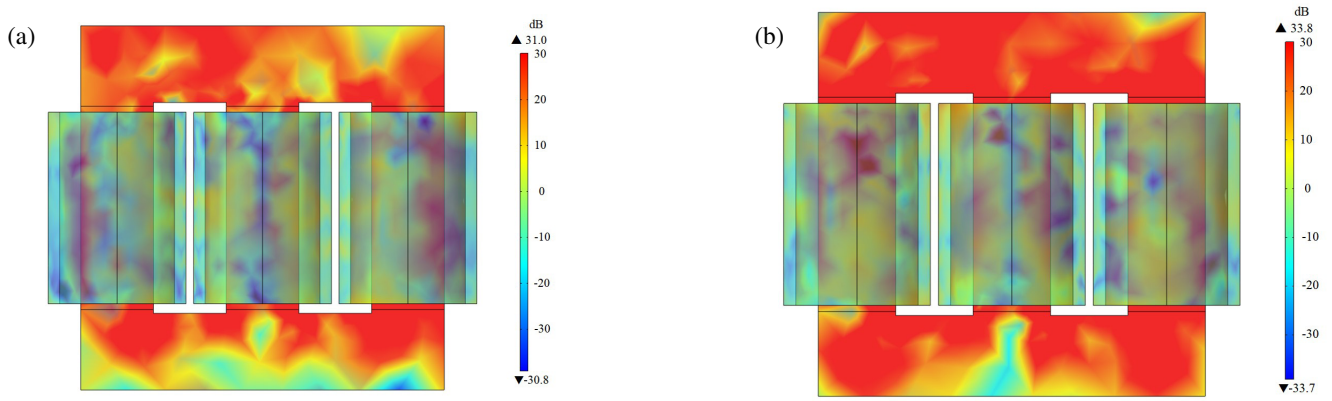

FIGURE 12. Maximum sound pressure level distribution. (a) m0 mode, (b) m3 mode.

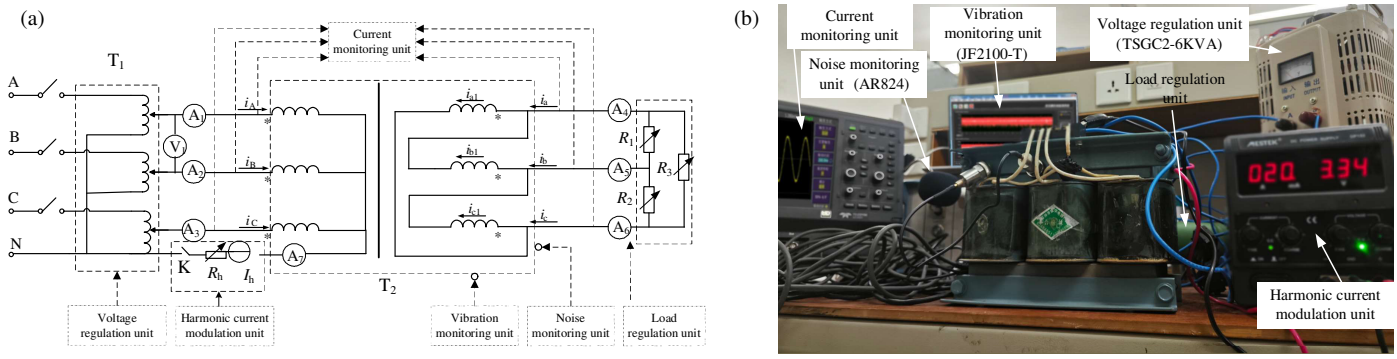

FIGURE 13. Experimental platform. (a) Experimental wiring, (b) Experimental diagram of transformer.

of winding mainly depend on the current. During full-load operation, although the amplitude of winding current is significant, the minor contribution of harmonics leads to negligible changes in vibration and noise. When the harmonic proportion reaches 10%, the amplitude of the winding vibration acceleration is about 1.2 times that of the normal operation, and the noise increases by 8%. The vibration and noise at the terminal of winding are more obvious than the middle part under the same condition.

(2) Transformer takes unstable performance of excitation saturation with harmonic invasion. As the harmonic proportion increases, the degree of excitation saturation gets serious, which aggravates the vibration and noise. When the harmonic proportion reaches 10% during full-load operation, the amplitude of winding vibration acceleration is about 1.3 times of normal operation. The results show that the core is more susceptible to harmonic invasion under the same condition. Additionally, the main heart column vibrates more intensely than the side columns.

5. EXPERIMENTS

Take the three-phase three-column experimental transformer (BSS-1kVA 35V/220V) as an example, the dynamic experiment platform is built, as shown in Fig. 13. Port current is collected in real time by setting different operating modes and adjusting the current monitoring unit (ZDS2022). The vibration information of components is obtained by using piezoelectric acceleration sensors and vibration monitoring unit (JF2100-T). According to the standard of transformer noise monitoring [21], transformer noise is monitored through the noise monitoring unit (AR824).

The transformer parameters are shown in Table 1. The primary side of the transformer is connected to the harmonic current modulation unit to simulate harmonic invasion. While the secondary side is connected to the vibration and noise detection unit to collect the data of transformer in different modes.

In order to verify the simulation conclusions, the transformer test points are consistent with the simulation. The vibration information of test points ① and ② is shown in Fig. 14.

In Fig. 14, when $\beta = 100\%$, the $g_{\max}$ at test points ① and ② in m2 mode is about 1.2 times that of m0 mode. Under full-load operation, the $g_{\max}$ of the winding in m1 mode increases by about 15% compared to that of the m0 mode. Actually, many factors exist in the experiment, including structural linkages, external environmental interference, and measurement errors. As a result, the measured vibration data is more complex than simulation results. However, the experimental variation law of the winding is basically consistent with the simulation results. As the I_h frequency, harmonic proportion, and β increase, the impact on the windings is more significant.

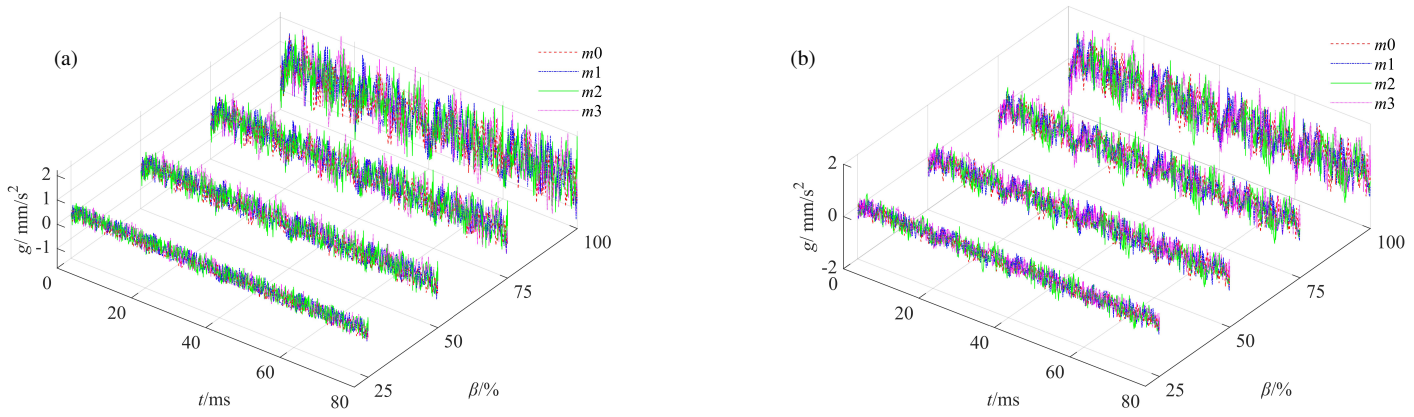

FIGURE 14. Experimental information of winding vibration. (a) Test point ①, (b) test point ②.

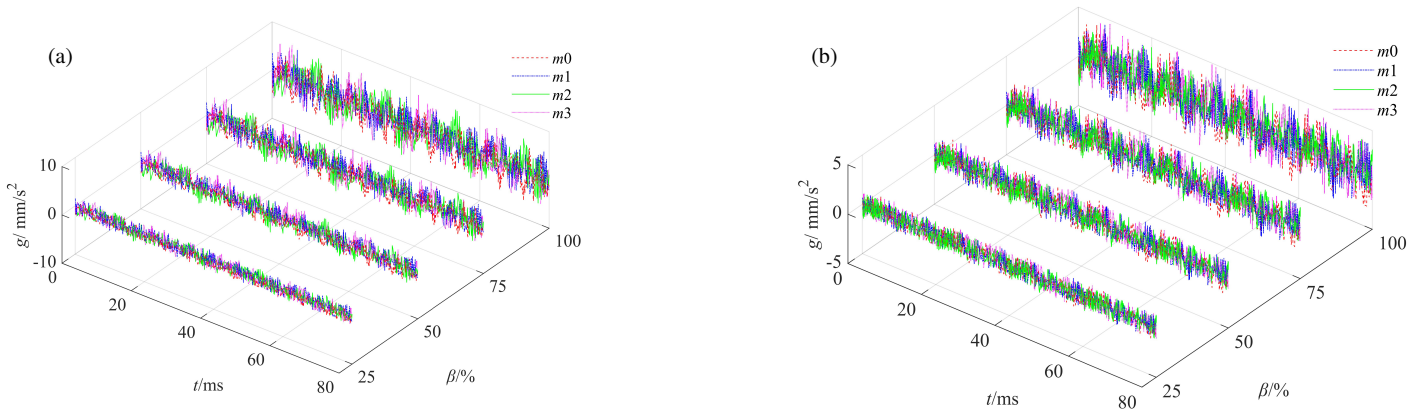

FIGURE 15. Experimental information of core vibration. (a) test point ③, (b) test point ④.

The vibration information of iron core is shown in Fig. 15. The iron core vibrates most intensely in m3 mode. Under full-load operation, the $g_{\max}$ of test points ③ and ④ in m3 mode is about 1.4 times that of m0 mode. The experimental results indicate that the core vibration is more pronounced than that of the winding with I_h invasion. However, the law of variation is similar.

Actually, external interference and measurement errors complicate the experimental results compared to simulation. However, the multi-field information of different components has similar variation law. Taking the test point ③ of the iron core as an example, simulation and experimental error analysis of the vibration acceleration is carried out. The variation of the error δ (%) (see Eq. (20)) is shown in Table 4.

$$\delta(\%) = \frac{|M_{h\_e} - M_{h\_s}|}{M_{h\_e}} \times 100\% \tag{20}$$

where $M_{h\_}e$ and $M_{h\_}s$ are the experimental and simulation data amplitudes in m0–m3 modes, respectively.

The simulated and experimental results of the transformer core vibration amplitude are within 5% error. The results show the accuracy of the transformer finite element model constructed, which can correctly reflect the variation law of multi-field information.

TABLE 4. Simulated and experimental vibration amplitude errors.

Vibration \ Scenario	Mode-state	β/%			
		25	50	75	100
Errorδ(%)	m0	2.43	3.02	2.41	2.76
	m1	3.31	2.85	3.92	3.01
	m2	3.08	4.57	4.17	3.97
	m3	4.10	3.62	4.85	1.93

Noise monitoring results of transformer are shown in Table 5. The noise of transformer in m3 mode is about 1.1 times that of the m0 mode. The variation of measured data is consistent with the variation law in simulation. The results show that noumenon noise of transformer is significantly enhanced with I_h invasion. Meanwhile, the noise level of transformer will be improved due to an increase of load factor.

Taking the transformer body noise as an example, the variation of error δ (%) with comparing the experimental results with the simulation ones is shown in Table 6.

The error of simulation and experiment results of transformer noise sound pressure level is less than 5%. It is shown that the transformer simulation model constructed is correct.

TABLE 5. Maximum experimental noise.

Noise \ Scenario Information	Mode-state	β/%			
		25	50	75	100
$L_{p\,\max}$ (dB)	m0	29.4	29.7	31.3	31.9
	m1	29.7	30.5	31.6	32.8
	m2	30.5	31.5	32.4	33.9
	m3	31.8	32.3	33.8	34.8

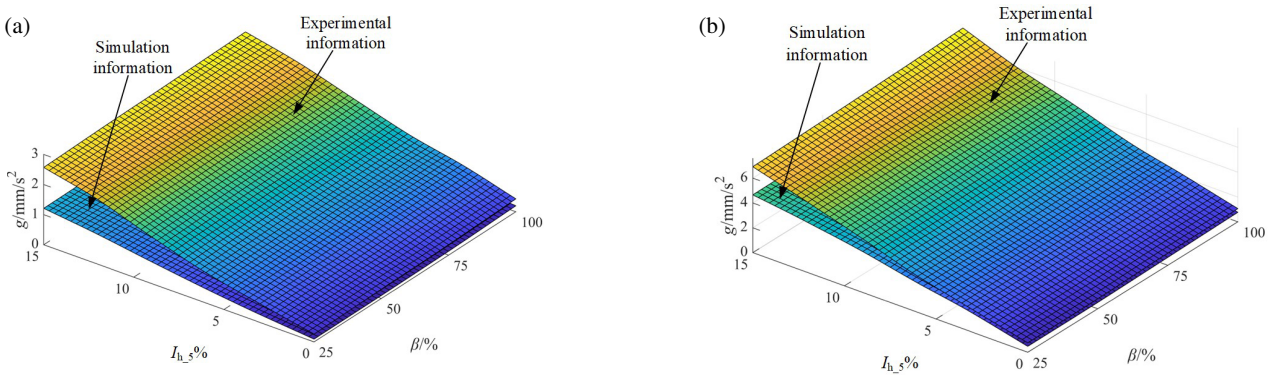

FIGURE 16. Electromagnetic-vibration information. (a) Test point ①, (b) test point ③.

TABLE 6. Simulated and experimental vibration amplitude errors.

Vibration \ Scenario	Mode-state	β/%			
		25	50	75	100
Errorδ(%)	m0	3.89	2.32	3.61	2.96
	m1	3.83	2.87	3.68	3.71
	m2	3.95	3.27	2.17	2.97
	m3	3.10	3.42	3.65	2.83

6. INSTABILITY CRITERION BASED ON FEATURE INFORMATION MAPPING

6.1. Instability Criterion

Related research indicates that in offshore wind power, the proportion of the 5th harmonic I_{h_5}% is the highest, and its duration is the longest. Therefore, it has the most serious impact on transformer [21].

Consequently, taking the proportion of the 5th harmonic I_{h_5}% as the characteristic parameter, the instability criterion of transformer feature information mapping is analyzed.

Taking the winding as an example, the component of vibration signal in the 100 Hz frequency band accounts for a larger proportion [22]. The vibration acceleration of the test points is deeply analyzed by selecting $g_{\_100\,\mathrm{Hz}}$ as the fingerprint quantity. The electromagnetic-vibration information mapping relationship of test points ① and ③ is shown in Fig. 16 (the mapping relationship of test points ② and ④ is shown in Appendix C).

It is easy to see that the multi-field feature information domains of different test points have similar distribution laws. Thus, the mapping relationship of feature information can be further investigated. The nonlinear mapping relationship between vibration acceleration and harmonic proportion is expressed in the form of mathematical function.

The critical parameters affecting the mapping relationship are mainly the load factor and the proportion of harmonic.

Taking the half-load mode in Fig. 16 as an example, the mapping function of I_{h_5}% to g is fitted as follows (see Appendix C for other details). The mapping parameters are shown in Table 7.

$$f(\beta, I_{h\_5}\%) = p_1(I_{h\_5}\%)^3 + p_2(I_{h\_5}\%)^2 + p_3(I_{h\_5}\%) + p_4 \quad (21)$$

TABLE 7. Nonlinear mapping parameters.

$f(\beta, I_{h\_5}\%)$	p_1	p_2	p_3	p_4
Simulation of test point ①	−0.0003	0.0047	0.0463	0.0975
Experiment of test point ①	−0.0004	0.0068	0.0395	0.1326
Simulation of test point ③	0.0032	−0.0213	0.4373	0.4125
Experiment of test point ③	0.0036	−0.0269	0.5697	0.5756

A similar mapping relationship of the g-I_{h_5}% is observed in different load modes, which is consistent with information domain distribution. Combined with the monitoring data and disturbed condition of equipment, the instability criterion is established with I_{h_5}% as the characteristic parameter:

$$I_{h\_5}\% = K_{\mathrm{rel}} I_{h0\_5}\% \quad (22)$$

It is experimentally demonstrated that when I_{h_5}% reaches 15%, the transformer exhibits exceptionally severe vibration

and noise, accompanied by insulation burnout phenomenon. Therefore, the safe working limit $I_{h0\_5}\%$ is taken as 15%, and the reliability coefficient K_{rel} is 1.1.

Taking half-load mode for example, when $0 \leq I_{h\_5}\% < 5\%$, the transformer is less disturbed by harmonics. At this point, the transformer is in stable operating condition. When $5\% \leq I_{h\_5}\% < 15\%$, the vibration and noise of component are serious. Although the effects of harmonic invasion can be endured by transformer, the cumulative effect of vibration and environmental noise pollution can no longer be ignored. At this point, the transformer is in a state of risk alert. When $I_{h\_5}\% \geq 15\%$, the normal operation of the transformer is seriously affected by harmonics. The staff should be alerted, and relevant suppression measures should be taken promptly.

In actual operation, transformer generally takes load factor lower than 75%. Although the proportion of harmonic remains within safety limits, the electromagnetic compatibility and structure stability of transformer have been significantly compromised. Especially, equipment is vulnerable to the harsh effects of harmonic invasion by the persistence and randomness of offshore wind power harmonics. Therefore, the anti-interference ability of the transformer needs to be improved, and the relevant treatment measures need to be further improved.

6.2. Management Strategy

Through the in-depth study of the characteristics of harmonic current interference, a novel management strategy is proposed, as shown in Fig. 17. The detection control module is connected in parallel at the neutral point of the transformer, so that the circuit is unidirectionally grounded. Then, the harmonic variations are monitored in real-time by integrating a harmonic monitoring and control system. When the harmonic exceeds the set value, it indicates that the safety and stability of the transformer is at risk. At this point, the management of harmonic is realized by disconnecting switch K_2.

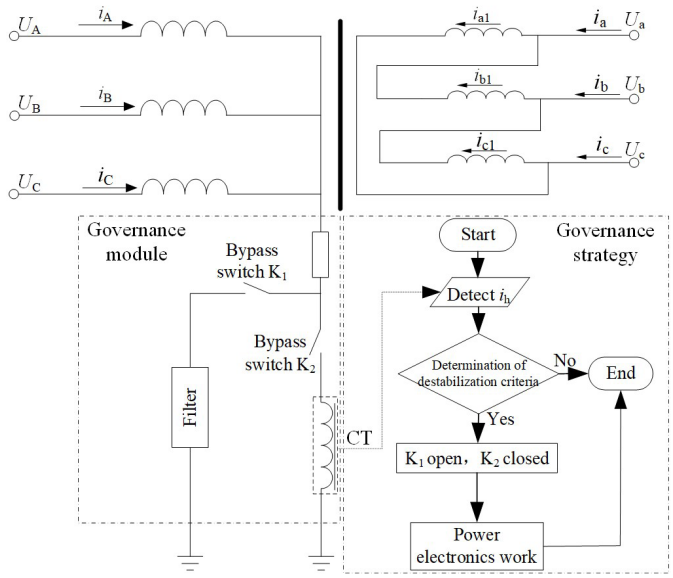

FIGURE 17. Harmonic current management strategy.

7. CONCLUSION

For the harmonic invasion in offshore wind power, the electromagnetic-solid-acoustic response of transformer and the variation of multi-field information parameters are researched. The conclusions are as follows:

(1) With harmonic invasion, the multi-field information in the transformer is significantly changed. The vibration and noise of the transformer intensify with the harmonic component for the same load mode. When the 5th harmonic proportion reaches 10% in full load mode, the amplitude of winding vibration acceleration is about 1.2 times that of normal operation, and the noise increases by 8%. Moreover, the vibration of iron core is about 1.3 times that of normal operation, and the noise increases by 3%. As the load factor of the transformer increases, vibration and noise become more severe under the same harmonic invasion mode. The vibration acceleration of the components during full-load operation is about 3 times that of 25% light-load operation. Under the same condition, the disturbed situation of the iron core is more serious than the winding. Additionally, the degree of abnormality in vibration and noise at the winding terminals is particularly significant. The correctness of the simulation analysis and conclusions is verified by the virtual/real consistency validation.

(2) Electromagnetic, solid and acoustic information of transformer with harmonic invasion can be related by multi-field information extraction method. Then, the implied mapping relationship is revealed by the fusion of anomalous feature information. Difficult-to-measure unusual vibration and noise can be represented by measurable harmonic currents and load factors. On this basis, we formulate the instability criterion by combining the disturbance of components, which provides an important basis for the development of risk-resistant auxiliary decision-making. The harmful effects of harmonic on transformer performance are clarified, which provides significant theoretical support for the maintenance of offshore wind farms. Furthermore, the information extraction method is helpful for studying the impact of harmonic effects, so that measures can be taken to improve the performance of the power equipment.

ACKNOWLEDGEMENT

The authors of this paper would like to thank the National Key R&D Program of China (2021YFB2400800) for their strong support.

APPENDIX A.

$$G_A = G_x + G_y + G_z \tag{A1}$$

$$\begin{bmatrix} G_x \\ G_y \\ G_z \end{bmatrix} = \int_\omega \frac{1}{\mu} \begin{bmatrix} \frac{\delta M_w}{\delta x}\left(\frac{\delta A_x}{\delta x}+\frac{\delta A_y}{\delta y}+\frac{\delta A_z}{\delta z}\right) \\ \frac{\delta M_w}{\delta y}\left(\frac{\delta A_x}{\delta x}+\frac{\delta A_y}{\delta y}+\frac{\delta A_z}{\delta z}\right) \\ \frac{\delta M_w}{\delta z}\left(\frac{\delta A_x}{\delta x}+\frac{\delta A_y}{\delta y}+\frac{\delta A_z}{\delta z}\right) \end{bmatrix} dV + \int_\omega \frac{1}{\mu} \begin{bmatrix} \frac{\delta M_w}{\delta y}\left(\frac{\delta A_y}{\delta x}-\frac{\delta A_x}{\delta y}\right)-\frac{\delta M_w}{\delta z}\left(\frac{\delta A_x}{\delta z}-\frac{\delta A_z}{\delta x}\right) \\ -\frac{\delta M_w}{\delta z}\left(\frac{\delta A_z}{\delta y}-\frac{\delta A_y}{\delta z}\right)+\frac{\delta M_w}{\delta x}\left(\frac{\delta A_y}{\delta x}-\frac{\delta A_x}{\delta y}\right) \\ -\frac{\delta M_w}{\delta x}\left(\frac{\delta A_x}{\delta z}-\frac{\delta A_z}{\delta x}\right)+\frac{\delta M_w}{\delta y}\left(\frac{\delta A_z}{\delta y}-\frac{\delta A_y}{\delta z}\right) \end{bmatrix} dV \tag{A2}$$

FIGURE A1. Material parameters tension and compression test platform (FL4000).

where G_x, G_y, G_z are the directional components of G_A.

APPENDIX B.

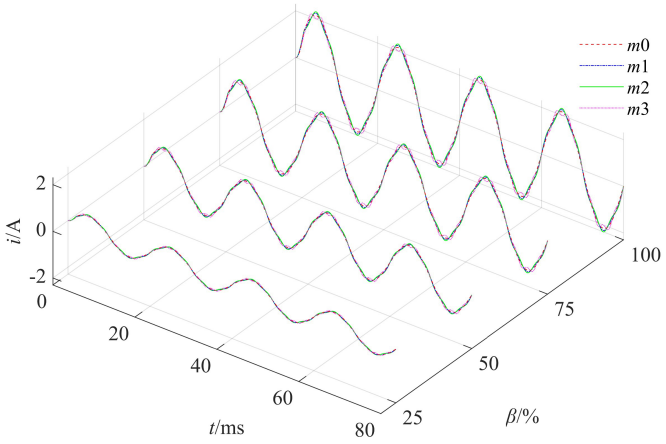

FIGURE B1. Simulation current data of phase B.

TABLE B1. Maximum transformer surface noise in various harmonic modes.

Interference mode / Parameters		I_h amplitude of the simulation and proportion (A/%)
harmonic-free	m0	0
2th harmonic	m12	0.09/5%
3th harmonic	m13	0.09/5%
3th harmonic	m1	0.09/5%

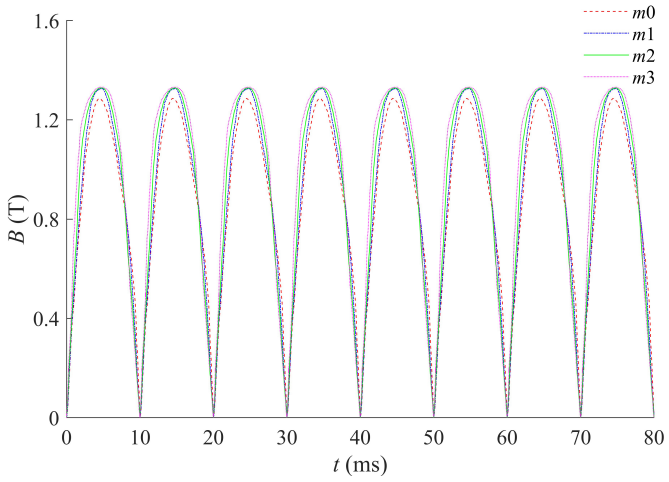

FIGURE B2. Main magnetic density of phase B, β =100%.

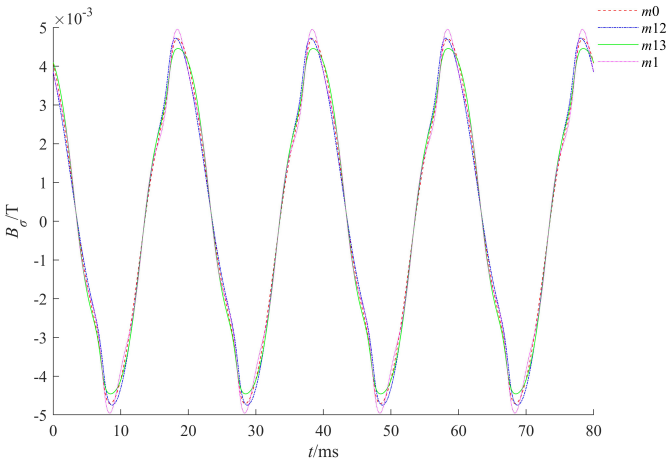

FIGURE B3. Variation law of leakage flux at test point ① under various harmonic, β =100%.

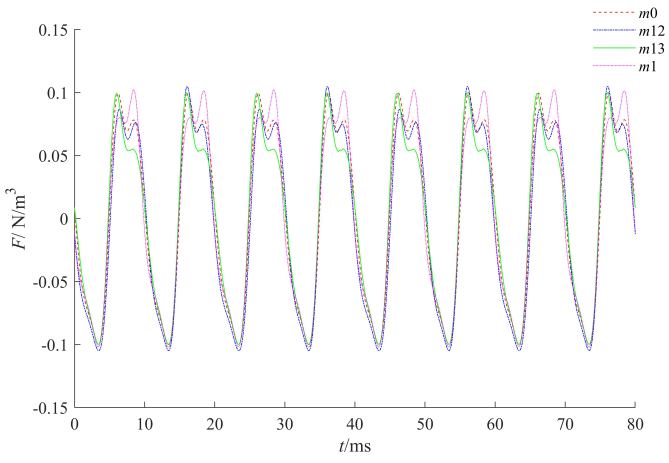

FIGURE B4. Variation law of force at test point① under various harmonic, β =100%.

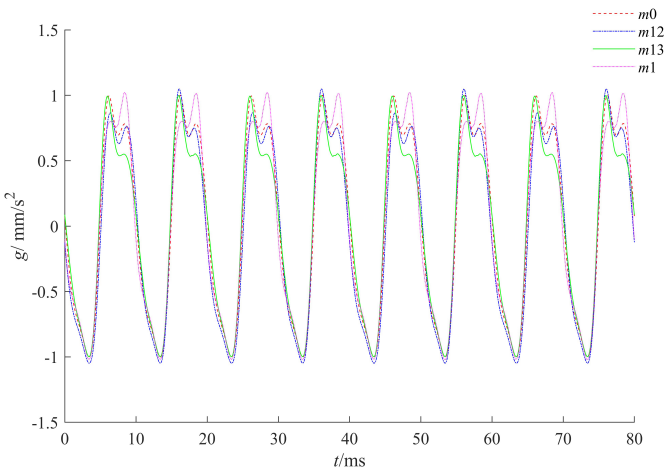

FIGURE B5. Variation law of vibration acceleration at test point ① under various harmonic, β =100%.

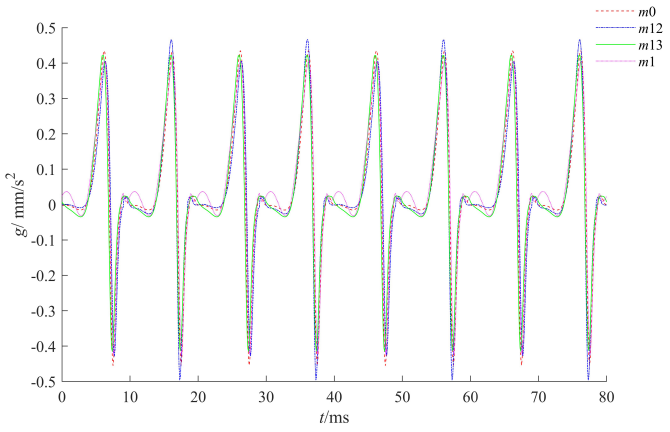

FIGURE B6. Variation law of vibration acceleration at test point ③ under various harmonic, β =100%.

TABLE B2. Maximum transformer surface noise in various harmonic modes.

Noise \ Scenario Information	Mode-state	β/%			
		25	50	75	100
$L_{p\,\max}$ (dB)	m0	28.3	29.0	30.2	31.0
	m12	28.3	29.1	30.2	31.2
	m13	28.5	29.4	30.3	31.5
	m1	28.6	29.6	30.5	31.6

APPENDIX C.

Parameters of the mapping relationship for $g - I_{h\_5}\%$ at β =25%:

TABLE C1. Mapping parameter.

$f(\beta,I_{h\_5}\%)$	p_1	p_2	p_3	p_4
Simulation of test point①	−0.0002	0.0055	0.0391	0.0919
Experiment of test point ①	−0.0003	0.0068	0.0479	0.0698
Simulation of test point ③	−0.0003	−0.0069	0.4608	0.2423
Experiment of test point ③	−0.0002	−0.0073	0.2283	−0.2204

Parameters of the mapping relationship for $g - I_{h\_5}\%$ at β =75%:

TABLE C2. Mapping parameter.

$f(\beta,I_{h\_5}\%)$	p_1	p_2	p_3	p_4
Simulation of test point ①	−0.0002	0.0051	0.0421	0.1274
Experiment of test point ①	−0.0001	0.0044	0.0503	0.1395
Simulation of test point ③	0.0003	−0.0031	0.4542	0.5174
Experiment of test point ③	0.0002	−0.0028	0.4175	0.6533

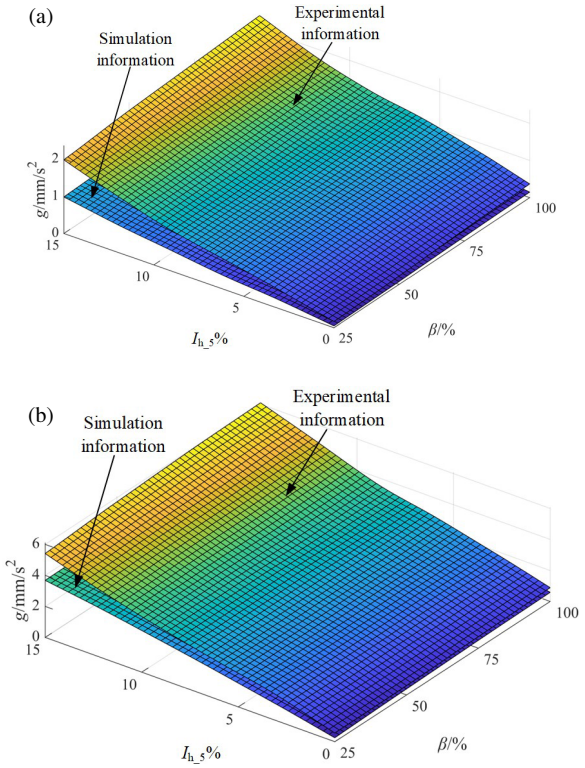

FIGURE C1. Electromagnetic-vibration information mapping relationship. (a) Test point ②, (b) test point ④.

Parameters of the mapping relationship for $g - I_{h\_5}\%$ at $\beta = 100\%$:

TABLE C3. Mapping parameter.

$f(\beta, I_{h\_5}\%)$	p_1	p_2	p_3	p_4
Simulation of test point ①	−0.0003	0.0043	0.0479	0.1644
Experiment of test point ①	−0.0002	0.0075	0.0536	0.1579
Simulation of test point ③	−0.001	0.0294	0.5153	0.5901
Experiment of test point ③	−0.001	0.0185	0.3748	0.7330

REFERENCES

[1] Tao, S., X. Zhu, S. Xu, and Y. Xu, "Modeling of coupled harmonic current source for grid-connected inverters," *IEEE Transactions on Power Electronics*, Vol. 39, No. 10, 13 720–13 732, Oct. 2024.

[2] Jiang, Z. and Y. Liu, "On the feasibility of harmonic adaptability remote testing method," *IEEE Transactions on Instrumentation and Measurement*, Vol. 69, No. 10, 8156–8166, Oct. 2020.

[3] Refaie Ali, A., H. O. Roshid, S. Islam, and A. Khatun, "Analyzing bifurcation, stability, and wave solutions in nonlinear telecommunications models using transmission lines, Hamiltonian and Jacobian techniques," *Scientific Reports*, Vol. 14, 15282, 2024.

[4] Wang, C., J. Fang, X. Liao, X. Wang, Y. Zan, and Z. Xiao, "Study on the influence of HTS strip and harmonics on AC loss of HTS transformer," *IEEE Transactions on Applied Superconductivity*, Vol. 34, No. 8, 1–4, Nov. 2024.

[5] Liu, Q., F. Liu, Y. Yang, Y. Peng, K.-Z. Liu, and A. Wang, "A novel transformer winding design strategy for efficiency improvement and harmonic suppression in industrial power system," *Protection and Control of Modern Power Systems*, Vol. 9, No. 6, 30–41, 2024.

[6] Gong, W., Z. Zhang, R. Hou, H. Wang, Z. Xu, A. Lin, J. He, W. Fan, and J. Wang, "Magnetostriction and the influence of harmonics in flux density in electrical steel," *IEEE Transactions on Magnetics*, Vol. 51, No. 11, 1–4, Nov. 2015.

[7] Xu, F., H. Zheng, H. Li, Z. Ma, and Q. Shu, "Study on the quantitative relationship between harmonic amplification and cable length," *IEEE Access*, Vol. 8, 152 611–152 619, 2020.

[8] Zhang, S., S. Jiang, X. Lu, B. Ge, and F. Z. Peng, "Resonance issues and damping techniques for grid-connected inverters with long transmission cable," *IEEE Transactions on Power Electronics*, Vol. 29, No. 1, 110–120, Jan. 2014.

[9] Wang, C., J. Fang, X. Liao, X. Wang, Y. Zan, and Z. Xiao, "Study on the influence of HTS strip and harmonics on AC loss of HTS transformer," *IEEE Transactions on Applied Superconductivity*, Vol. 34, No. 8, 1–4, Nov. 2024.

[10] Pejovski, D., K. Najdenkoski, and M. Digalovski, "Impact of different harmonic loads on distribution transformers," *Procedia Engineering*, Vol. 202, 76–87, 2017.

[11] Cheah-Mane, M., L. Sainz, E. Prieto-Araujo, and O. Gomis-Bellmunt, "Impedance-based analysis of harmonic instabilities in HVDC-connected offshore wind power plants," *International Journal of Electrical Power & Energy Systems*, Vol. 106, 420–431, 2019.

[12] Kocewiak, L. H., I. A. Aristi, B. Gustavsen, and A. Holdyk, "Modelling of wind power plant transmission system for harmonic propagation and small-signal stability studies," *IET Renewable Power Generation*, Vol. 13, No. 5, 717–724, 2019.

[13] Kalair, A., N. Abas, A. R. Kalair, Z. Saleem, and N. Khan, "Review of harmonic analysis, modeling and mitigation techniques," *Renewable and Sustainable Energy Reviews*, Vol. 78, 1152–1187, 2017.

[14] Islam, S., B. Halder, and A. R. Ali, "Optical and rogue type soliton solutions of the (2+1) dimensional nonlinear heisenberg ferromagnetic spin chains equation," *Scientific Reports*, Vol. 13, 9906, 2023.

[15] Pan, C., S. Yi, H. Su, and W. Shi, "Excitation–vibration harmonic response research of transformer in DC biasing operation," *IET Electric Power Applications*, Vol. 13, No. 3, 410–417, 2019.

[16] Zhao, X., C. Yao, C. Zhang, and A. Abu-Siada, "Toward reliable interpretation of power transformer sweep frequency impedance signatures: Experimental analysis," *IEEE Electrical Insulation Magazine*, Vol. 34, No. 2, 40–51, Mar.–Apr. 2018.

[17] Refaie Ali, A., N. T. M. Eldabe, A. E. H. A. E. Naby, M. Ibrahim, and O. M. Abo-Seida, "EM wave propagation within plasma-filled rectangular waveguide using fractional space and LFD," *The European Physical Journal Special Topics*, Vol. 232, No. 14, 2531–2537, 2023.

[18] Yang, X.-J., A. A. Alsolami, and A. R. Ali, "An even entire function of order one is a special solution for a classical wave equation in one-dimensional space," *Thermal Science*, Vol. 27, 491–495, 2023.

[19] Refaie Ali, A., M. N. Alam, and M. W. Parven, "Unveiling optical soliton solutions and bifurcation analysis in the space-time fractional Fokas-Lenells equation via SSE approach," *Scientific Reports*, Vol. 14, 2000, 2024.

[20] IEC 60076-10, "Power transformers-part 10: Determination of sound levels," *International Standard*, 2001.

[21] Guest, E., K. H. Jensen, and T. W. Rasmussen, "Mitigation of harmonic voltage amplification in offshore wind power plants by wind turbines with embedded active filters," *IEEE Transactions on Sustainable Energy*, Vol. 11, No. 2, 785–794, 2020.

[22] Wang, Y., L. Li, J. Sun, and X. Zhao, "A magnetic-mechanical strong coupling FEM model and vibration characteristic analysis of transformer core under DC bias," *Journal of Applied Physics*, Vol. 134, No. 24, 244504, Dec. 2023.